Cell Differentiation-Inspired, Salt-Induced Multifunctional Gels for an Intelligent Soft Robot with an Artificial Reflex Arc

Huijing Li, Long Li, Hao Zhang, Junjie Wei,* Zhenyu Xu, and Tao Chen*

ACCESS | Metrics & More | Article Recommendations | SI Supporting Information

ABSTRACT: To make soft robotics intelligent, dazzling artificial skin and actuators have been created. However, compared to rigid commercial robots, the sophisticated demands of raw materials become a key challenge for autonomous soft actuators to realize manufacturing repeatability and reproducibility. Inspired by the stem cell, which has the potential to differentiate into multifunctional cells with the same original compositions, a potential multifunctional gel is presented. With well-designed polymer chains, the gel has a salt-induced regulating module, conductivity, and other bionic properties. Making use of this advantage, the gel acts as a double-duty electrode for both the actuator and sensor. An artificial reflex arc is therefore formed by their tight integration via an e-brain: a computing unit that specifically responds to organism intervention. This efficient strategy to obtain diverse components with minimal raw materials is promising for effortlessly fabricating fully soft robotics.

KEYWORDS: cell differentiation, multifunctional gel, intelligent soft robot, artificial reflex arc, dielectric elastomer actuator

INTRODUCTION

One of the amazing capabilities that enables the human body to respond to surroundings is the reflex, which is realized by the cooperation of sensing functions, neural signal processing, and motor responses.[1] The emulation of this process becomes a promising technology in bioinspired electronics for intelligent robotics. For example, to produce the bionic electric skin, there are numerous skilled designs in both structure and materials for accurate and efficient stimuli sensing.[2−5] Meanwhile, various artificial muscles based on asymmetric expansion,[6,7] pneumatic inflation,[8−12] and hydraulic actuation[13,14] with specific system programming were developed, for instance. Consequently, in terms of mimicking biological conditioned reflex, which receives external stimuli and produces informative synaptic-responsive and motor outputs, the complex and incompatible production processes of electric skins and artificial muscles lead to high production costs and delicate preparation of intelligent robotics.[15,16] Therefore, one of the key challenges in the field of commercial intelligent soft robotics construction is developing a kind of novel multifunctional intelligent material for an efficient manufacturing process.

On the contrary, in the human body, multifunctional tissues and organs are all originally differentiated from stem cells under specific stimuli,[17,18] such as muscles and skin, which are responsible for actuating and sensing (Figure 1A). This mechanism guarantees that biological metabolism is efficient in working and recovering while facing changing situations (e.g., injuries). The differentiation process inspired us to believe that if the actuator and sensor were designed with the same composition in one robotic system, this would significantly promote the design of intelligent robotics with simplified and efficient manufacturing. Nevertheless, the soft actuator and the sensor always have different, even opposite, material demands, for instance, mechanical properties and conductivities. Coincidentally, gels are attractive bionic materials for soft robotics with their three-dimensional (3D) polymer networks, whose properties can be regulated via interaction between polymer chains.[5,19,20] They have also been developed with multiple properties similar to biological tissues (e.g., self-healing ability and stretchability). Thus, we herein draw inspiration from the cell differentiation process to develop a salt-induced multifunctional gel (SIMG), which can serve as both an actuator and a sensor with the same sandwich-shaped structure. Furthermore, an intelligent close-loop actuating system with an artificial reflex arc was fabricated successfully by employing the as-fabricated gel-based actuator and sensor, showing biomimetic automatic actuation adapting to environmental change without the manipulation of humans.

The SIMG applied here is synthesized based on the polymer that consists of a hydrophilic part, a hydrophobic part, and charged side chains on the backbone. The diverse interactions between polymer chains can be adjusted by adding conductive
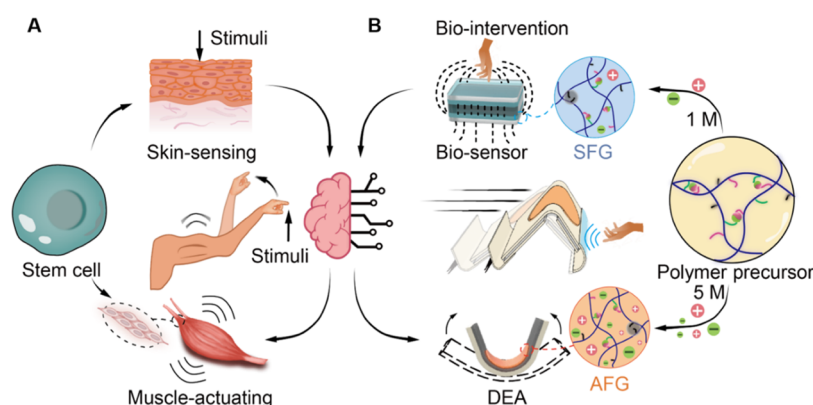
Figure 1. Efficient soft robot manufacturing design with salt-induced multifunctional gel inspired by cell differentiation. (A) Example of the cell differentiation process. The stem cell differentiates into skin cells and muscle cells, which play roles as sensors and actuators in conditioned reflexes. (B) Design of the soft robot with salt-induced multifunctional gels. Actuating-functional gel (AFG) and sensing-functional gel (SFG) were prepared by adding different salt contents to the polymer precursor. After that, they were integrated into a sandwich-shaped dielectric elastomer actuator (DEA) and sensor, which constructed an intelligent soft human-avoidance vehicle.
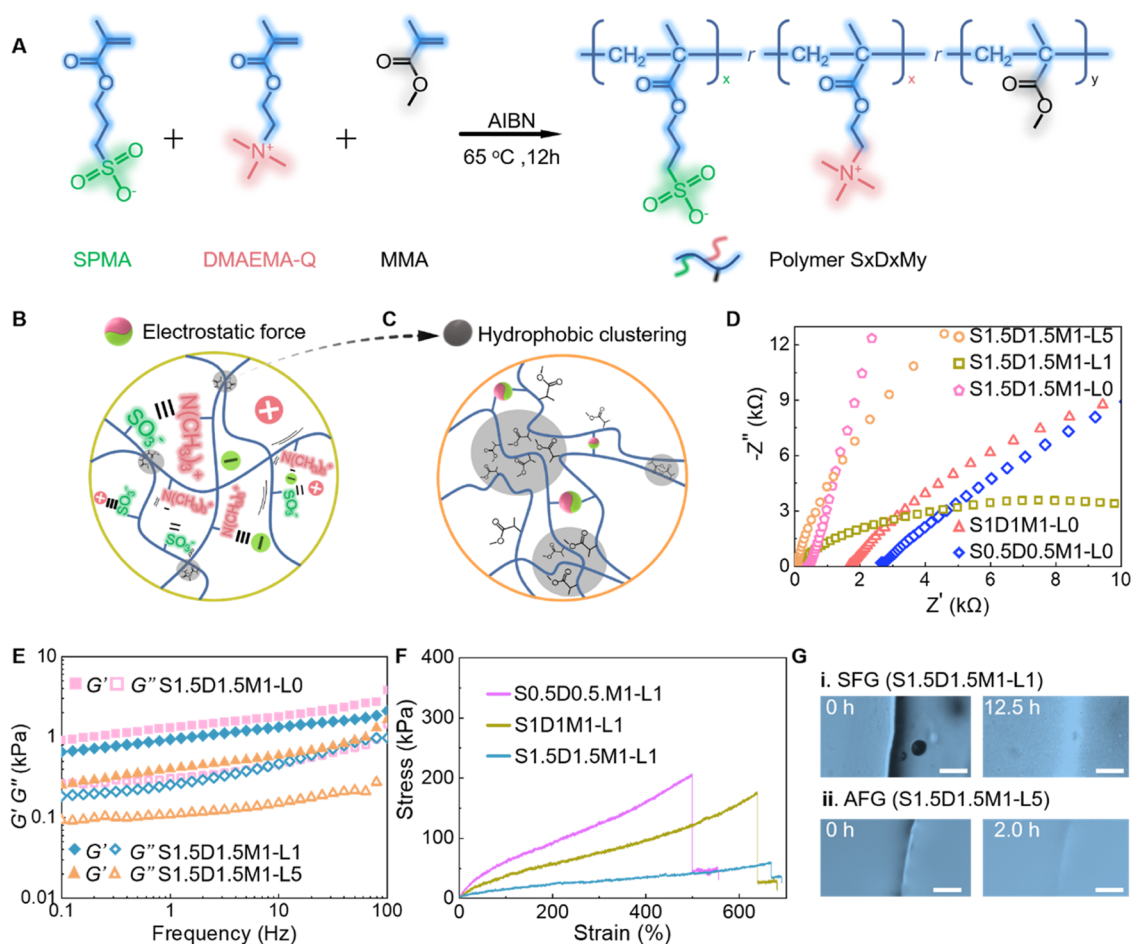

Figure 2. Fabrication and characterization of SIMG. (A) Schematic illustration of the SxDxMy polymer design. Scheme for electrostatic force (B) and hydrophobic clustering of polymer chains caused by the part in polymer chains that gathers in the oil phase (C). (D) Comparison of conductivities of series SIMGs. (E) Frequency dependencies of the storage (G') and loss (G'') moduli of SIMGs with different LiCl contents (S1.5D1.5M1-L0, S1.5D1.5M1-L1, and S1.5D1.5M1-L5 gels). (F) Tensile tests of the gels with different MMA ratios. The higher the MMA ratio, the higher the Young modulus of the gel. (G) Self-healing performance of SFG and AFG in the ambient atmosphere (scale bars = 100.0 μm).

salt (LiCl). It also endows SIMG with regulated moduli, stretchability, and self-healing ability. Afterward, the SIMGs were integrated successfully into a sandwich-shaped gel-based dielectric elastomer actuator (DEA) and a capacitive biosensor as electrodes. The similar constituent of the actuator and sensor facilitates the manufacturing with the fewest raw materials but not compromising their soft and functional properties. The DEA with the advantages of high actuation strain, high energy density, and high energy conversion efficiency requires a low-modulus but high-conductivity electrode,[21−23] which was obtained using

high salt content and named the actuating-functional gel (AFG). For accurate and efficient sensing, the capacitive sensor needs a higher-modulus gel electrode with low salt content, which was named the sensing-functional gel (SFG). These two coinciding parts were combined with the help of the e-brain (computing unit) to realize the intelligent artificial reflex arc with autonomous motor responses to organisms' intervention (Figure 1B).

RESULTS

Fabrication and Characterization of SIMG. For optimizing SIMGs' mechanical and conductive performances, a series of polymers for gel networks were first synthesized with an anionic monomer [3-sulfopropyl methacrylate potassium salt (SPMA)], a cationic monomer ([(Methacryloxy)ethyl]-trimethylammonium chloride (DMAEMA-Q)), and a hydrophobic monomer [methyl methacrylate (MMA)] by free-radical polymerization in the specific ratios of 0.5:0.5:1 (S0.5D0.5M1), 1:1:1 (S1D1M1), and 1.5:1.5:1 (S1.5D1.5M1) (Figure 2A and Table S1). Polymers' chemical structure and composition were confirmed using ^{1}H NMR spectra (Figure S1).

The polymer was first dissolved in a dilute aqueous solvent consisting of hygroscopic organic liquid glycerol (5.0 wt %) and water to get the basic precursor of SIMG. After adding LiCl, the 80 °C thermal-drying process was conducted for the strong physical cross-linking between polymer chains rather than with solvent molecules, and the stable gel was formed.[24] The addition of hygroscopic salt LiCl plays an essential role in inducing properties to change, for instance, conductivity, wet adsorption, and mechanical properties. Here, we increased the LiCl content from 0 to 1.0 and 5.0 mmol/L, and the SIMG samples were named SxDxMy-L0, SxDxMy-L1, and SxDxMy-L5, respectively. Consequently, there are electrostatic forces (Figure 2B) and hydrophobic clustering (Figure 2C) between polymer chains since there are charged side chains on the backbone and the hydrophobic part.

The interaction between polymer chains in the hydrophilic part is affected by LiCl as well (Figure 2B). The electrostatic force coincides with Fourier transform infrared (FT-IR) spectra (Figure S2), in which the peak related to asymmetric stretching of sulfate groups ($\approx$1150 cm^{-1}) and ammonium groups ($\approx$3400 cm^{-1}) shifted to lower wavenumbers ($\approx$1000, 3280, respectively) with increasing content of LiCl.

This phenomenon indicates that physical cross-linking was partly replaced by the interaction between either sulfate groups and Li$^+$ or ammonium groups and Cl$^-$; namely, the addition of LiCl weakens the electrostatic force between polymer chains.[2] The conductivities are also affected by the addition of LiCl, besides the ratio of the hydrophilic part in polymer chains (Figure 2D). The conductivities of S0.5D0.5M1-L0, S1D1M1-L0, S1.5D1.5M1-L0, S1.5D1.5M1-L1, and S1.5D1.5M1-L5 are 5.0×10^{-4}, 7.9×10^{-4}, 3.6×10^{-3}, 1.5×10^{-2}, and 2.2×10^{-2} S/m, respectively. The reason is that the presence of dominant conductive ions (Li$^+$ and Cl$^-$) further increases the SIMG's conductivities based on the increasing content of ionic side chains in hydrophilic parts. Moreover, since mechanical properties are influenced by physical cross-linking density, LiCl can therefore regulate mechanical properties. However, if there is too much LiCl in the precursor, it would be hard to form a solid gel owing to fewer cross-linking sites. As shown in Figure 2E, with the same polymer network, the higher the salt content, the lower the storage moduli. The S1.5D1.5M1-L5 gel shows the lowest storage modulus (484.6 Pa) among all samples, while

S1.5D1.5M1-L0 exhibits the highest storage modulus (3.1 kPa), and S1.5D1.5M1-L1 stays in the middle (2.0 kPa).

Meanwhile, because of the different solubilities between monomers (SPMA, DMAEMA-Q, and MMA) and solvents (water and glycerol), the existence of MMA in polymer composition changes its hydrophobicity and causes phase separation in the precursor (Figure 2C). Thus, polymer chain clusters appear in the oil phase, which can be easily distinguished with scattered shadows in the transmission electron microscopy (TEM) image (Figure S3) and atomic force microscopy (AFM) phase image (Figure S4) of the S1.5D1.5M1-L0 gel. These polymer chains result in stronger polymer—polymer interaction than polymer—solvent interaction in the aqueous system, which is helpful for gelation during the thermal-drying process. Moreover, the clusters reflected in the roughness measured using AFM (Figure S5) can mainly be responsible for its mechanical properties such as Young's modulus and elasticity. With decreasing MMA content, the SIMGs of S0.5D0.5M1-L1, S1D1M1-L1, and S1.5D1.5M1-L1 exhibited Young's moduli of 70.0 kPa, 41.4 kPa, and 16.1 kPa, respectively (Figure 2F). At the same time, according to the rheological characterization, the order of storage modulus (G') values is S0.5D0.5M1-L1 > S1D1M1-L1 > S1.5D1.5M1-L1, which agrees well with the results of the tensile test (Figure S6).

After comprehensively considering the SIMGs' conductive and mechanical properties, high conductivity is the first condition of being an excellent electrode, so polymer S1.5D1.5M1 was chosen as the skeleton of SIMG with massive ionic side chains. After that, the moduli of SIMGs were also considered. For electrodes of DEA, S1.5D1.5M1-L5 with high conductivity and low elastic modulus (compliance) satisfies the demand.[21,25] As to electrodes of capacitance sensors, a suitable elastic property is needed, ensuring excellent recovery ability during the sensing process for accurate signal monitoring. On the contrary, low modulus would strengthen pressure sensing, which causes proportional capacitance change, while weakening the organism's contact sensing resulting from electrical field change, namely, the inversely proportional capacitance change.[26] That is why S1.5D1.5M1-L1 is ideal for capacitance sensor electrodes. As a result, S1.5D1.5M1-L5 acted as AFG and S1.5D1.5M1-L1 acted as SFG.

For long-term stable working of AFG and SFG, self-healing and antidrying abilities are also essential. As shown in Figure 2G, SFG and AFG exhibit self-healing properties in the ambient atmosphere, whose cut traces disappear at around 12.5 and 2.0 h, which result from dynamic electrostatic cross-linking sites in gels and relatively low moduli. From the tensile test, the self-healing efficiency of SFG reaches 70.2% within 30.0 min in terms of maximum strength (Figure S7A). The self-healing performance of AFG was further confirmed by the conductivity measurement. The conductivity of the AFG gel recovers in 30.0 s after cutting (Figure S7B). With the assistance of hygroscopic organic liquid glycerol and hygroscopic salt LiCl, after 4.0 h of thermal ageing, the gels (SFG and AFG) reached their equilibrium states (Figure S8) with 20.0 and 40.0% water contents (Figure S9), respectively. After that, the water content remains stable. This means the existence of glycerol and LiCl preserves gels from drying by moisture adsorption. AFG kept higher water content since there was more hygroscopic salt LiCl in the gel.

Actuator Design and Performance. The essential requirement to be electrodes of DEA is that they must firmly adhere to the dielectric film (VHB tape) to prevent slippage between the electrode and VHB during actuation and to provide
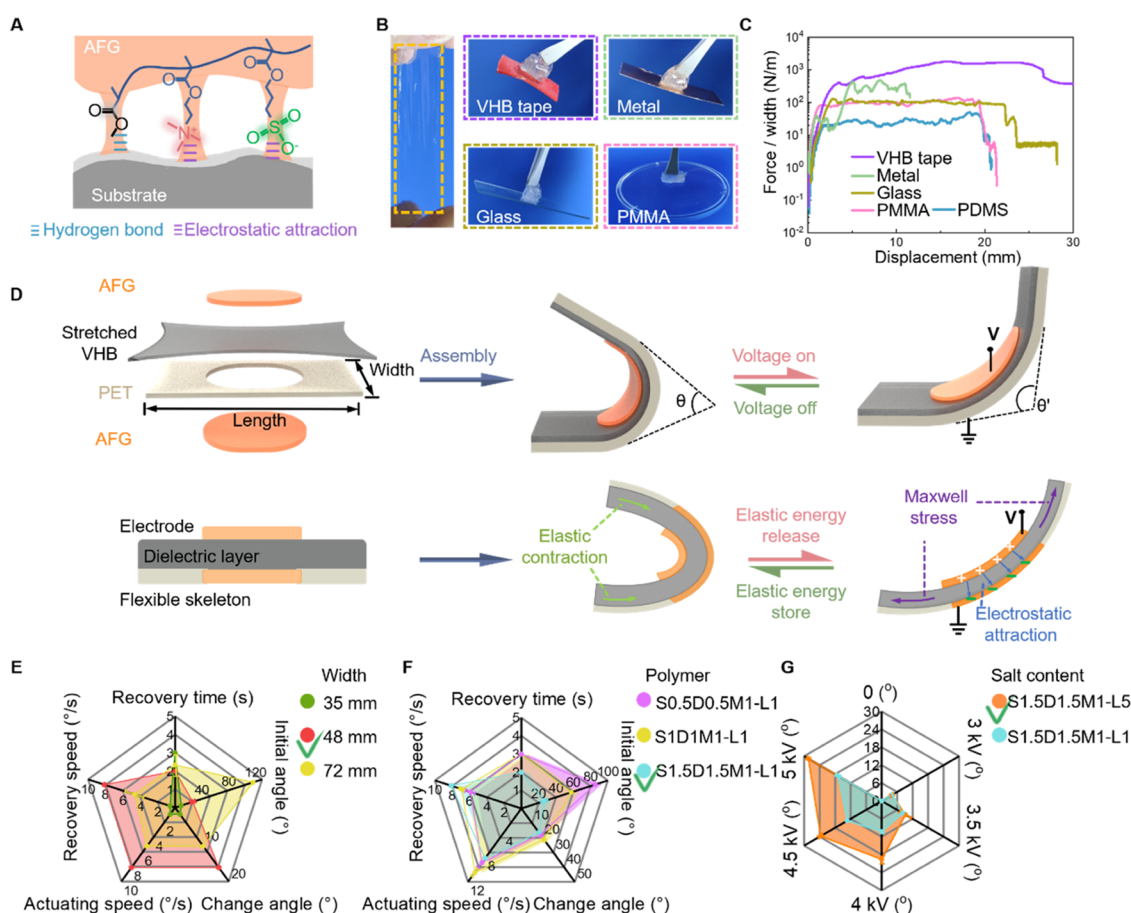
Figure 3. Actuator design and performance. (A) Schematic illustration of AFG adhered to the substrate through intermolecular bonds. (B) Photos of the AFG gel and its attachment with VHB tape, metal, glass, and PMMA. (C) 90° peeling-off curves of AFG adhered to the above substrates. (D) Schematic illustration of the actuator fabrication process and front view of its operating mechanism. Synthetical actuating performance of the actuator with (E) series skeleton width, (F) electrodes of various polymer networks, and (G) different salt contents (error bars represent the standard deviation (SD) for $n = 5$ measurements at each data point).

mechanical integrity for the overall assembly.[21] Owing to the noncovalent bonding formed by polar groups of polymer side chains, including hydrogen bonds and electrostatic attractions to various substrates, as shown in Figure 3A, AFG could attach to VHB tape, metal, glass, poly(methyl methacrylate) (PMMA), and poly(dimethylsiloxane) (PDMS) (Figure 3B). We further evaluated the adhesion properties of the AFG gel through the 90° peeling-off test (Figure S10) and summarized the interface force of these gel−substrate adhesions. Generally, hydrophobic VHB is hard to stick to the hydrogel with high water content. However, as shown in Figure 3C, the AFG composite has a peeling force per unit width of 1944.4 N/m with VHB tape, which is the toughest among these substrates due to the great noncovalent bonding force between VHB tape and AFG gel. The peeling forces on metal, glass, PMMA, and PDMS substrates are 288.2, 104.8, 83.7, and 27.2 N/m, respectively, on average.

To improve the ultimate working performance of DEA-based robots, we need a DEA with suitable locomotion properties. The detailed fabrication process of the actuator is shown in Figure 3D. A thin gel film (about 300.0 μm) was stuck on both sides of a prestretched ($400 \times 400\%$) dielectric layer (VHB 4910) to form a DEA with a poly(ethylene terephthalate) (PET) skeleton (length: 85.0 mm).

After assembling, the actuator stores elastic energy without applying voltage and creates a buckle-shaped bend with the initial angle (θ) as the elastic contraction of VHB. When the voltage is applied, positive or negative charges accumulate in electrodes, inducing electrostatic attraction and Maxwell stress that release the elastic energy of VHB, which deforms VHB. The net effect is an increase in the body angle of the PET skeleton to an actuating state (θ'). The deformation with or without voltage is reversible.

To find the optimal PET skeleton size for the actuator, we fabricated skeletons of three widths. We evaluated their performance in terms of the initial angle, changed angle, actuating speed, recovery speed, and recovery time. The changed angle is defined as the difference between the initial angle (θ) and actuating state angle (θ').

As shown in Figure 3E, with the fixed length of 85.0 mm and the same actuating voltage (5.0 kV), we compared actuator performance with skeletons of 35.0, 48.0, and 72.0 mm widths. Among these actuators, the 48.0 mm width skeleton has a moderate initial angle (25.4°) and the most significant changed angle (16.2°) in 5.0 s. At the same time, its actuating and recovery speeds are as fast as 8.1 and 8.2°/s, respectively, which means that it recovers to its initial state in 1.9 s. While the 35.0 mm width skeleton is too small to be used in our applications (initial angle, 8.7°; changed angle, 1.8°; actuating speed, 0.9°/s; recovery speed, 0.6°/s; recovery time, 3.0 s) and the 72.0 mm width skeleton cannot bend adequately in the initial state (initial
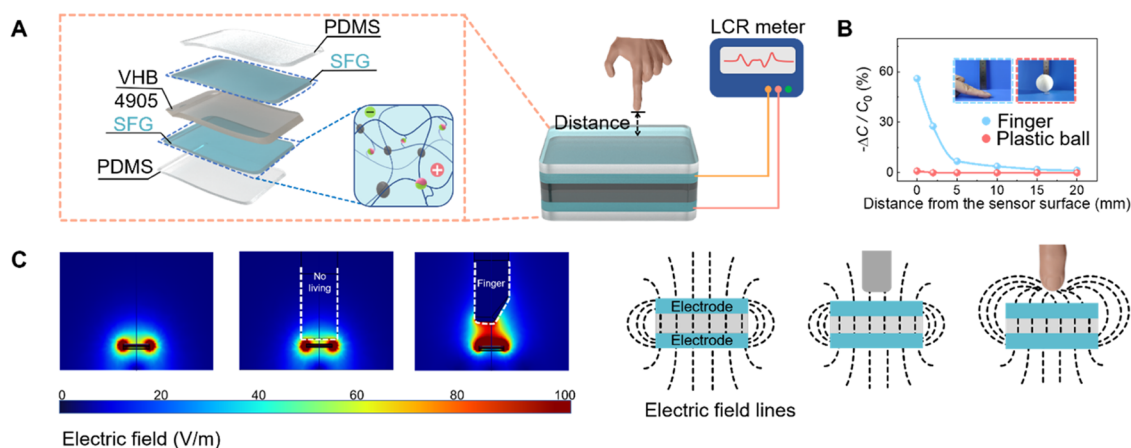
Figure 4. Sensor design, working mechanism, and application. (A) Schematic diagram of the sensor design and measurement. (B) Change in capacitance upon the approach of a finger and plastic ball. (C) Simulated results of electric field distributions under the proximity of different things.

angle, 116.4°; changed angle, 10.5°; actuating speed, 5.2°/s; recovery speed, 4.6°/s; recovery time, 2.3 s).

These differences are mainly affected by the response torque of the skeleton.[27] The response torque of the skeleton can be derived as

$$T_S = \frac{E(w - 2r)t^3}{12s}(\pi - \theta) \tag{1}$$

where E is Young's modulus of the skeleton, w is the width of the skeleton, r and s are the radius and width of the hollow area at the center, as shown in Figure S11, and t is the thickness of the skeleton. With fixed E, r, t, and s, the width value is proportional to the response torque. When the actuator stays at its initial state, there is an equilibrium between skeleton torque and VHB torque. Since the stretch ratio of VHB is fixed at 400 × 400%, this equilibrium state mainly depends on the PET skeleton width in this comparison experiment, which means the wider the skeleton, the harder it is to bend in its initial state. During actuation, the bending angle changes. With a larger bending angle (θ), PET shows smaller torque and thus slower actuating and recovery speeds. Meanwhile, the initial angle of the skeleton in 35 mm width is too small, which means in its initial state, the torque of VHB is so strong that the actuation and recovery are difficult. To sum up, the skeleton with an 85.0 mm length and a 48.0 mm width was chosen for further actuator performance investigation.

To further confirm that S1.5D1.5M1-L5 is the best choice of AFG, we compared the actuating performance of DEAs with the above gel as electrodes. First, the influence of electrode moduli on actuating state was tested with gels of different polymer networks. Their performances are shown in Figure 3F. The most significant difference among these actuator performances is their initial angle and recovery time. The actuator with S0.5D0.5M1-L1 electrodes has an initial angle as large as 86.1°, while the actuator with S1D1M1-L1 electrodes has a smaller initial angle (57.5°). The actuator with S1.5D1.5M1-L1 electrodes has the lowest initial angle of about 25.4°. They have decreasing changed angles and similar actuating speeds (S0.5D0.5M1-L1, 20.7°, 8.8°/s; S1D1M1-L1, 18.1°, 10.4°/s; S1.5D1.5M1-L1, 16.4°, 8.1°/s), while S1.5D1.5M1-L1 has fast recovery speed (8.2°/s) and minimal recovery time (2.0 s). This is because the high Young's modulus of electrodes would impede the recovery process after the voltage is cut off. After cutting off the voltage, without Maxwell force, an actuator with soft electrodes is easier

to recover to its initial state, which coincides with the initial state and outstanding recovery performance of the actuator with S1.5D1.5M1-L5 electrodes.

During the actuation and recovery process, the conductivity of the electrode also decides the actuating and recovery states. According to the actuating angle comparison shown in Figure 3G, an actuator with S1.5D1.5M1L-5 gel electrodes has more obvious deformation than an actuator with S1.5D1.5M1-L1 gel electrodes because of higher conductivity (Figure 2D). Higher conductivity means more charge accumulation in electrodes during the voltage on condition; namely, more significant Maxwell force works on VHB. All actuating states under increasing voltage were evaluated after charging in 5.0 s.

The above phenomenon proved S1.5D1.5M1-L5 as the best choice of AFG with the 85.0 mm length and 48.0 mm width PET skeleton for its appropriate initial and changed angles and fast recovery speed.

Besides, the DEA with AFG electrodes also had superior stability (Figure S12) and antimechanical abrasion ability (Figure S13), and the actuating process was conducted for 100 cycles with the PET frame (Figure S14).

Organism Sensor Design and Application. The organism sensor was designed based on a mutual capacitance sensor, which is less susceptible to the noise environment distribution and the change in air circulation.[28−30] The freestanding sensor comprised two SFG electrodes separated by a dielectric layer (VHB 4905) (Figures 4A and S15). The electrodes were covered by thin PDMS films (200.0 μm) for better tactile impression and reduced electrode damage during application. The capacitance was measured by an LCR meter. To confirm the organism proximity detection capability of the sensor, we vertically moved the finger closer to the sensor. Figure 4B shows the relative magnitude of the change in capacitance as a function of distance from the surface with a finger and table tennis ball approach, which is defined as

$$-\Delta C/C_0 = -\frac{C - C_0}{C_0} \tag{2}$$

where C represents the actual time capacitance and C_0 is the initial capacitance at the relaxed state (the sensor with lateral dimensions of 10.0 mm × 30.0 mm). In this test, the table tennis ball represented a nonliving object. The change in capacitance decreased when the finger was far from the surface but was still significant even at 10.0 mm. At the same time, the proximity of
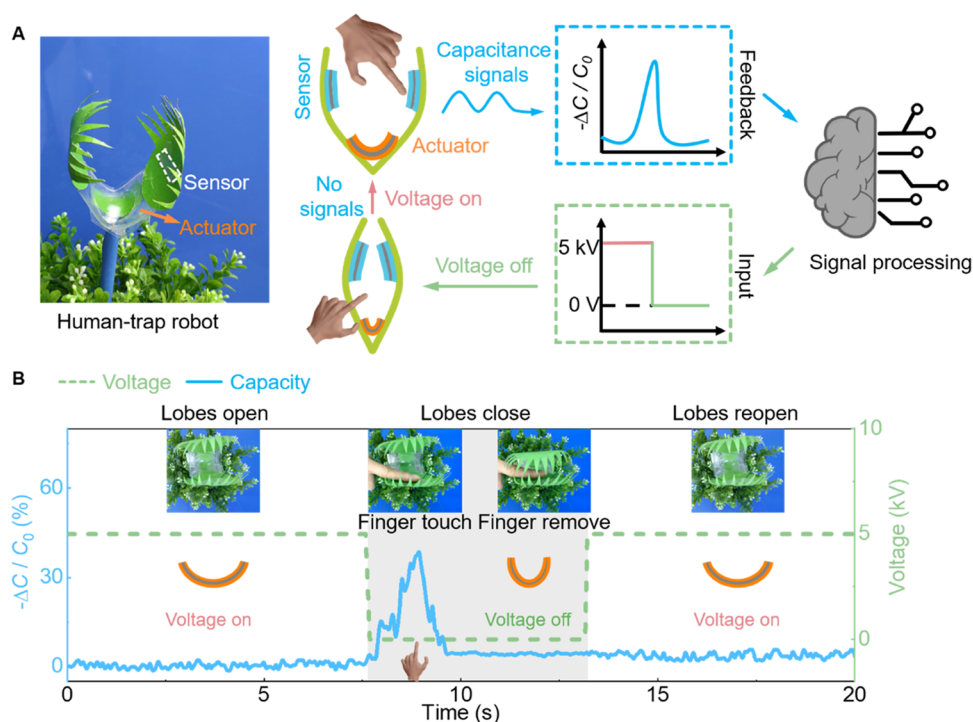
Figure 5. Human-trap robot design and performance. (A) Photograph of the human-trap robot with sensor and actuator components and the cooperative working process between the sensor and the actuator. Once a human touched the sensor on the lobe, a capacitance change was recognized by the signal processing unit. After that, the voltage was switched off and the robot closed its lobes. (B) Measured relative capacitance change and voltage change during the interaction.

the table tennis ball did not affect the capacitance, which means a nonliving object would not change the capacitance of the sensor without contact. To understand this better, we have simulated the capacitance change with three different models in COMSOL: no-proximity, nonliving object-proximity, and finger-proximity. As shown in Figure 4C, in the finger-proximity model, the electric field lines around the finger increase and become dense, as seen in the red area around the finger. The electric field is increasingly directed toward the finger, decreasing the charges shared between the two electrodes and thus declining the capacitance.[26] In contrast, the nonliving object approach does not lead to a change of electric field around capacitance, which means that its contact would not affect the capacitance. Simulation results demonstrate that the sensor can determine human proximity and touch.

The sensing phenomena under various stimulations were further investigated. Since pressure deformation, the capacitance increased when the pressure was applied to the sensor. According to the relationship between deformation and capacitance in a parallel-plate configuration

$$C = \frac{\varepsilon S}{4\pi k d} \tag{3}$$

where C is the capacitance, ε is the dielectric constant of the dielectric layer, k is the electrostatic constant, S is the effective area of the conducting layer, and d is the thickness of the dielectric layer. For the nonliving object, because the electric field lines would not be influenced by them, the only way to change the capacitance value is to change the shape of the sensor. When applying pressure to the sensor, an expanding area leads to an increased capacitance, which may disturb human sensing. However, the detectivity of mechanical deformation is too weak (Figure S16) to interfere with organism sensing

(Figure S17). The interesting phenomenon is that due to the electrical conductivity of the metal, it can adapt to the electric field around the sensor rather than change it, so its proximity would not affect the capacitance. However, the capacitance would suddenly decline when a human touched the metal weight that was placed on the sensor because the electric field was changed by the human via the conductivity of the metal (Figure S18A,B). As shown in Figure S18C,D, both finger proximity (1.0 cm) and touch decreased the capacitance, consistent with Figure 4B. The response time during finger touch is as short as 33.0 ms, defined as the time from finger touch to a 90.0% increase in relative capacitance change. The decrease of capacitance with finger touch is still significant and stable for 200 cycles (Figure S19).

These results showed that our organism-sensing device could accurately and rapidly detect human-representing proximity and touch, even under mechanical deformation.

Based on our sensor's distinguished human-sensing performance, it could potentially be applied in an intelligent remote control vehicle. By combining our human sensor with a vehicle driving system, the vehicle can be intelligently controlled by human proximity (Figures S20 and S21). As depicted in Figure S22A, the sensor acts as a controller of the driving system. When a human approaches the controller (almost 1.0 cm), it will output a signal with a relative capacitance change over a threshold, and the vehicle will receive a deceleration order. Once the human moves away, the speed will increase to its initial value. As can be seen in Figure S22B and Movie S1, when there is no human disturbance, the capacitance change keeps stable at 0, and the vehicle travels at high speed. There is an apparent decrease in capacitance change when the finger gets close, which causes the vehicle to slow down, as shown in Figure S22C and Movie S2.
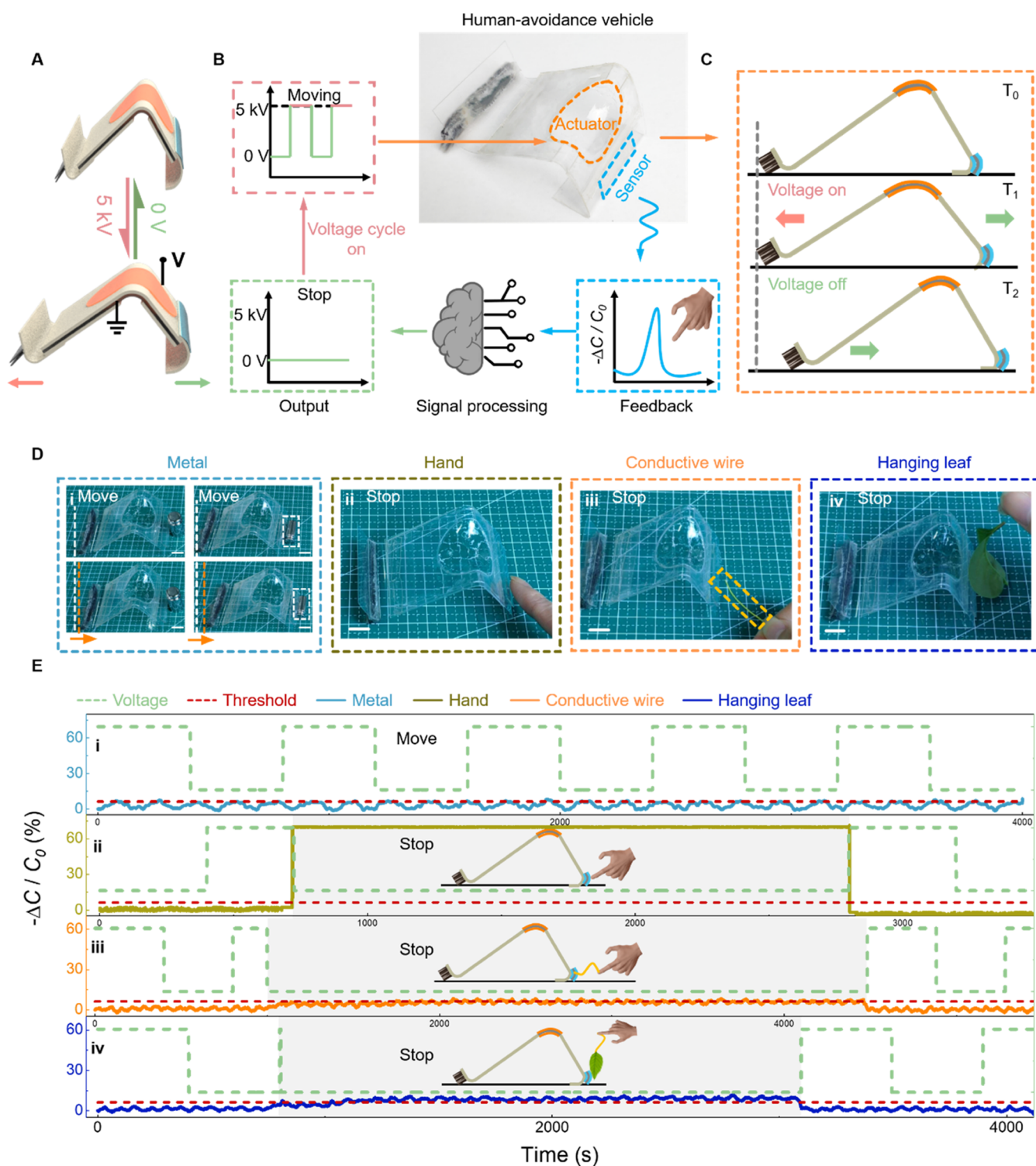
Figure 6. Human-avoidance vehicle design and performance. (A) Schematic diagram of the vehicle locomotion with voltage on or off. (B) Photograph and working principle of the human-avoidance vehicle. (C) Working process when the vehicle moves forward. (D) Photographs of the vehicle when it met with (i) metal weight, (ii) hand, (iii) hand holding a conductive wire, and (iv) hand holding a hanging leaf. (E) Measured capacitance and voltage change when the vehicle met the above obstacles.

Human-Interactive DEA-Based Robots. Moreover, we devised two distinct human-interactive DEA-based robots by combining our coincided DEA and the sensor based on the SIMG. The organism sensor worked as a sensory neuron to accurately receive human contact signals and deliver them to the computing unit (i.e., central nervous system), which further transferred it to the actuating order of DEA (i.e., motor neuron).

The computing unit can be edited with the desired program to endow DEA with a distinct working model, which helps us utilize this system in various functional situations, for instance, a bioinspired human-trap robot and a human-avoidance vehicle.

Inspired by the prey-recognizing predation performance of flytraps, a human-trap robot was constructed, whose structure is shown in Figure 5A. The invisible and adhesive human sensor is

attached to the lobes, which are symmetrically fixed on the end of the DEA skeleton. As depicted in Figure 5A, when the sensor is stimulated by human touch and outputs a signal with a noticeable capacitance change, the generated signals are transmitted to the Arduino module for signal processing. After that, the input voltage suddenly turns off and causes lobes to close immediately, which protects humans from contact with high voltage (Figure S23). Once the stimulation disappears, namely, stop touching the sensor, 5 s later, it reopens with 5.0 kV voltage and is ready for the next cycle. The 5.0 kV voltage is chosen for stability and repeatability in the case of dielectric breakdown.

As shown in Figure 5B and Movie S3, in the beginning, the capacitance change was so stable around 0 that the lobes remained open. As the finger approached and eventually touched the sensor on the lobe, there was such a massive decline in capacitance that the voltage was abruptly cut off, and the lobes closed rapidly. Although the finger moved away from the lobe, the input voltage was still off for 5.0 s, and the lobes remained closed as preset, which imitates the predation mode of the flytrap. With capacitance keeping constant, lobes reopened and were ready for the next interaction. Furthermore, the human-trap robot remained functionally stable in air after two weeks (Figure S24). This human-trap robot presents a wide range of possibilities for developing a selective human-interactive robot. We further demonstrate its potential application as a soft human-avoidance vehicle. As mentioned above, a crucial part of safe driving is the ability to make a rapid reaction when facing pedestrians. Keeping effective interaction between environment and vehicles, such as stopping immediately when meeting with pedestrians, is a matter for self-driving automobiles. Our human-avoidance vehicle can realize this through the intelligent cooperation of organism sensors and self-driving automobiles. The vehicle consists of DEA as a soft motor and the sensor attached to the foreleg to detect humans. Self-driving is achieved by the cyclic motions between bending and unbending of the actuator (Figure 6A). As can be seen from Figure 6B, after inputting voltage (5.0 kV) with a frequency of 0.2 Hz, the vehicle moves forward (Figure 6C). When the sensor feeds back a stable, large value of capacitance change that over the threshold under stimulation, the Arduino module processes the signal, causing cyclic input voltage to turn off and the vehicle to stop at once.

Not only direct contact with humans but indirect human touch would trigger the vehicle's brake. To deeply investigate the human-avoidance ability of the vehicle facing various obstacles, metal weight, human hand, hand holding a conductive wire, and hand holding a hanging leaf were sequentially placed in front of the vehicle during moving. As we mentioned before, the metal weight cannot cause capacitance change, so the vehicle kept moving, even pushing the weight forward upon contact (Figure 6D-i). However, direct human contact made an apparent decrease in the capacitance, and the vehicle consequently stopped (Figure 6D-ii). What is more, indirect human touch via a conductor also stopped the vehicle. As shown in Figure 6D-iii,iv, we chose a soft conductive wire and a hanging leaf to act as conductive objects connected to humans, and these barriers resulted in the vehicle stopping effectively. Figure 6E shows the capacitance change and voltage change records. The capacitance change leveled around 4.0% when met with a metal barrier, whose fluctuation was caused by high-input-voltage electromagnetic radiation (5.0 kV). This unstable change could not reach the threshold, so the cyclic voltage kept inputting, and

the vehicle moved forward continuously (Figure 6E-i and Movie S4). However, when the hand appeared in front of the vehicle, the relative capacitance change showed a sharp increase from 0 to almost 70.0%, resulting in an abrupt voltage-off. The vehicle stopped until the hand left (Figure 6E-ii and Movie S5). Similarly, the flexible hand holding a conductive wire also contributed to a capacitance change of nearly 8.0%, which reached the threshold, and the voltage was cut off (Figure 6E-iii). Moreover, the leaf representing a living body also can act as a medium of human touch and has this brake effect as well (Figure 6E-iv). The leaf was hung via a conductive wire, which was held by a human. Once it got in touch with the sensor, a slight relative capacitance change of about 10.0% was noted, and the vehicle thus stopped in this case. The threshold of relative capacitance change, which determines whether to stop the vehicle, can be adjusted depending on the situation. Movie S6 presents more situations when different barriers hinder vehicle movement.

■ CONCLUSIONS

To fabricate intelligent soft robots with abilities of both sensing and actuating via an efficient manufacturing process, we have drawn inspiration from the differentiation process of stem cells to develop a SIMG. It can differentiate into AFG or SFG under salt stimulation. Taking advantage of AFG and SFG, the sensor and DEA with similar compositions and structures were tightly integrated with the assistance of an e-brain, the computing unit, which constructed a complete artificial reflex arc. When the e-brain was programmed with a certain motion discipline, the actuator would autonomously convert the desired working state facing human-representing organisms. Taking advantage of this system, two excellent human-interactive smart robots with distinct working models were further fabricated, realizing friendly interaction with humans.

This bioinspired manufacturing method of intelligent soft robotics is the crucial novel evolution for constructing fully soft robots in an efficient and operation-friendly way. Using an artificial reflex arc that starts from an organism-detecting sensor, many unique robot models could specifically interact with humans, which is greatly meaningful to the efficient human—robot interaction (HRI). The success of the application of this stimuli-induced multifunctional gel in soft robotics was expected to be a starting point for the exploration of more potential multifunctional unified robots that are greatly approaching natural organisms.

■ EXPERIMENTAL SECTION/METHODS

Materials. 3-Sulfopropyl methacrylate potassium salt (SPMA), [(methacryloxy)ethyl]trimethylammonium chloride (DMAEMA-Q), methyl methacrylate (MMA), 2,2′-azobis(2-methylpropionitrile) (AIBN), dimethyl sulfoxide (DMSO), methanol (MeOH), glycerol, and lithium chloride (LiCl) were purchased from Aladdin Shanghai Reagent Co. Ltd. AIBN was purified by recrystallization. Other materials were used without further purification. Deionized water was used in preparing the solution. VHB tapes (4905 and 4910) were purchased from Minnesota Mining and Manufacturing Corporation. Poly(dimethylsiloxane) (PDMS) (200.0 μm) was purchased from Hangzhou Bald Advanced Materials Co. Ltd. PET (0.18 mm) was obtained from Tongshi Co. Ltd.

Preparation of the Gels. The specific ratios of SPMA, DMAEMA-Q, MMA, and AIBN (Table S1) were used for polymerization in water/DMSO cosolvent (50/50 vol %) (at 65.0 °C, overnight). After that, polymers were precipitated in MeOH.

The polymers (150.0 mg) and LiCl (SxDxMy-L1, 21.2 mg; SxDxMy-L5, 106.0 mg) were dissolved in a 5 wt % aqueous glycerol

solution (50.0 mL), which consists of 2.5 mL of glycerol/47.5 mL of Di water. Next, the resulting solutions were drop-cast on the template (Teflon substrate) and then thermal-aged at 80.0 °C for 2.0 h.

Characterizations. [1]H nuclear magnetic resonance (NMR) spectra were recorded on a Bruker Advance III 400 MHz spectrometer in D_2O. The conductivity and electrical signals were recorded on the CHI660E electrochemical workstation (CH Instruments). Fourier transform infrared (FT-IR) spectra were taken on a Thermo NICOLET 6700 FT-IR spectrophotometer. The TEM images were recorded using a JEOL-2100 electron microscope. AFM measurements were conducted using a Dimension ICON SPM (Bruker) in Peak Force tapping mode. The rheological characterizations were performed on a Haake MARS III rheometer equipped with 25.0 mm diameter parallel plates, where frequency ω was set from 0.1 to 100.0 Hz at room temperature under a fixed strain amplitude of 1.0%. The tensile tests and adhesive properties were conducted on the Z1 Zwick/Roell Universal Testing System (Zwick). Tensile tests were performed at room temperature at 50.0 mm/min tensile speed. Samples were cut into dumbbell shapes (size: length × width × thickness, 50.0 mm × 5.0 mm × 0.5 mm). Adhesive properties were determined at a tensile speed of 50 mm/min with the strip shape (size: length × width × thickness, 50.0 mm × 10.0 mm × 0.5 mm). The images of the gel self-healing process were recorded using a TU-1810 UV−vis spectrophotometer provided by Purkinje General Instrument Co. Ltd. The water content of samples was measured by TGA (TGA 8000-Spectrum two-Clarus SQ8T), in which the rate of temperature increase was 2 °C/min. The applied voltage was provided by a benchtop power supply (DW-P303-1ACH2). The capacitance measurements were obtained using an LCR meter (TH 2830) at an AC voltage of 1.0 V and a sweeping frequency of 1.0 kHz. The LCR meter was used to detect simultaneous capacitive changes under various stimuli on the sensor. All of the patterned PET frames were obtained by a laser cutter (GY-460 bought from Shandong Liaocheng Guangyue Laser Equipment Co. Ltd.).

Theoretical Simulations of the Capacitive Sensor. The COMSOL software package was used to analyze the measuring process of the sensor. The SFG@PDMS elastic electrodes and the approaching object were considered conductors, which were applied at a certain electric potential of their boundary. The electric potential of the upper part of the sensor was 1 V, while the electric potentials of the lower part of the sensor and the approaching object were 0 V. The relative permittivity of the air around the sensor was 1. The relative permittivity of the dielectric layer was 3. The sensor was placed at the center of an infinite space, and the electric potential at the infinite boundary was 0.

Structure and Fabrication of a Human-Trap Robot. First, a primary frame was prepared by PET with an approximate elliptical hole (Figure S25A,B). Next, having chosen VHB 4910 as the DE film and stretching it with a biaxial prestrain of 400.0% in each direction, the film was attached to the PET skeleton. The AFG electrodes were assembled on both sides of the prestretched film and aligned with the frame hole to get an actuator.

Afterward, the above actuator was applied to the human-trap robot (Figure S25C). The sensors used here were cut in the size of 1.0 cm × 4.0 cm and attached to the lobes. Both lobes and the stem of the robot were prepared with colored papers. Eventually, all components were assembled by VHB 4905. A conductive copper wire was connected to the electrodes of the sensor and actuator by gels' stickiness.

Structure and Fabrication of a Human-Avoidance Vehicle. Initially, the soft motor of the human-avoidance vehicle was proposed, which is similar to the actuator of the human-trap robot. The different parts are the site of the elliptical hole on the PET skeleton and the addition of PET strengthen plates (Figure S25D,E). The location of the elliptical hole is close to one side of the frame rather than in the middle, which aims to shift the center of gravity forward during moving. The addition of PET strength plates further guarantees that the motor does not bend to a curve, maximizing the actuating force on the foreleg and hindleg. They were mounted on one side of the VHB opposite the PET skeleton.

If the friction between the hindleg and ground is not larger than that of the foreleg, the vehicle will slide in the start place; namely, it cannot move forward. We combined a row of brushes to the hindleg and bent the foreleg to the arc to improve the backward friction and decreasing the forward friction, as shown in Figure S25F. VHB 4905 plays the role of a sticker in assembling legs on the soft motor. The conductive copper wire was used the same way as the human-trap robot.

■ ASSOCIATED CONTENT

Ⓢ Supporting Information

The Supporting Information is available free of charge at https://pubs.acs.org/doi/10.1021/acsami.2c20172.

^{1}H NMR spectra of the SxDxMy polymer (Figure S1); FT-IR spectra of S1.5D1.5M1-L0, S1.5D1.5M1-L1, and S1.5D1.5M1-L5 (Figure S2); TEM image of FS1.5D1.5M1-L0 (Figure S3); AFM image of S1.5D1.5M1-L0 (Figure S4); AFM modulus image of S1.5D1.5M1-L0 (Figure S5); frequency dependencies of the storage (G′) and loss (G″) moduli of S0.5D0.5M1-L1, S1D1M1-L1, and S1.5D1.5M1-L1 (Figure S6); self-healing performance of SFG and AFG (Figure S7); weight change of SFG and AFG after thermal ageing (Figure S8); TGA curves of SFG and AFG in the equilibrium state (Figure S9); schematic diagram of the 90° peeling test (Figure S10); schematic diagram of the PET skeleton (Figure S11); stability of DEA (25 °C, 60% RH) (Figure S12); schematic diagram and photographs of the DEA antiabrasion process (Figure S13); reliable actuating performance of the actuator (Figure S14); photograph of the organism sensor (Figure S15); pressure sensing performance of the sensor (Figure S16); recorded relative capacitance change while being bent (Figure S17); capacitance changes in multiple situations (Figure S18); reliable human touch sensing performance of the sensor (Figure S19); circuit diagram between the wireless vehicle and controller (Figure S20); working principle between the wireless vehicle and the controller (Figure S21); performance of the intelligent environmentally friendly vehicle (Figure S22); construction components of the human-trap robot system (Figure S23); human-trap robot performance after 14 days (Figure S24); design and fabrication of robots (Figure S25); and ratio of monomers in polymers (Table S1) (PDF)

Intelligent vehicle at high speed without human interference (Movie S1) (MP4)

Intelligent vehicle at low speed with human approaching (Movie S2) (MP4)

Performance of the human-trap robot compared with the flytrap (Movie S3) (MP4)

Human-avoidance vehicle performance facing metal weight (Movie S4) (MP4)

Human-avoidance vehicle performance facing humans (Movie S5) (MP4)

Human-avoidance vehicle performance facing various barriers (Movie S6) (MP4)

■ AUTHOR INFORMATION

Corresponding Authors

Junjie Wei − *Key Laboratory of Marine Materials and Related Technologies, Zhejiang Key Laboratory of Marine Materials and Protective Technologies, Ningbo Institute of Material Technology and Engineering, Chinese Academy of Sciences, Ningbo 315201, China; School of Chemical Science, University of Chinese Academy of Sciences, Beijing 100049, China;*

◉ orcid.org/0000-0003-3403-4308; Email: weijunjie@nimte.ac.cn

Tao Chen — *Key Laboratory of Marine Materials and Related Technologies, Zhejiang Key Laboratory of Marine Materials and Protective Technologies, Ningbo Institute of Material Technology and Engineering, Chinese Academy of Sciences, Ningbo 315201, China; School of Chemical Science, University of Chinese Academy of Sciences, Beijing 100049, China;* ◉ orcid.org/0000-0001-9704-9545; Email: tao.chen@nimte.ac.cn

Authors

Huijing Li — *Key Laboratory of Marine Materials and Related Technologies, Zhejiang Key Laboratory of Marine Materials and Protective Technologies, Ningbo Institute of Material Technology and Engineering, Chinese Academy of Sciences, Ningbo 315201, China; School of Chemical Science, University of Chinese Academy of Sciences, Beijing 100049, China*

Long Li — *Key Laboratory of Marine Materials and Related Technologies, Zhejiang Key Laboratory of Marine Materials and Protective Technologies, Ningbo Institute of Material Technology and Engineering, Chinese Academy of Sciences, Ningbo 315201, China*

Hao Zhang — *School of Chemical Science, University of Chinese Academy of Sciences, Beijing 100049, China*

Zhenyu Xu — *Key Laboratory of Marine Materials and Related Technologies, Zhejiang Key Laboratory of Marine Materials and Protective Technologies, Ningbo Institute of Material Technology and Engineering, Chinese Academy of Sciences, Ningbo 315201, China; School of Chemical Science, University of Chinese Academy of Sciences, Beijing 100049, China*

Complete contact information is available at:
https://pubs.acs.org/10.1021/acsami.2c20172

Author Contributions

Methodology: H.L., L.L., H.Z., and Z.X. Investigation: H.L., L.L., H.Z., and Z.X. Data curation: H.L., L.L., snd Z.X. Writing—original draft: H.L. and J.W. Writing—review and editing: T.C.

Notes

The authors declare no competing financial interest.

■ REFERENCES

(1) Shih, B.; Shah, D.; Li, J.; Thuruthel, T. G.; Park, Y.-L.; Iida, F.; Bao, Z.; Kramer-Bottiglio, R.; Tolley, M. T. Electronic Skins and Machine Learning for Intelligent Soft Robots. *Sci. Rob.* **2020**, *5*, No. eaaz9239.

(2) Yu, Z.; Wu, P. Underwater Communication and Optical Camouflage Ionogels. *Adv. Mater.* **2021**, *33*, No. 2008479.

(3) Araromi, O. A.; Graule, M. A.; Dorsey, K. L.; Castellanos, S.; Foster, J. R.; Hsu, W. H.; Passy, A. E.; Vlassak, J. J.; Weaver, J. C.; Walsh, C. J.; Wood, R. J. Ultra-Sensitive and Resilient Compliant Strain Gauges for Soft Machines. *Nature* **2020**, *587*, 219−224.

(4) Qin, J.; Yin, L. J.; Hao, Y. N.; Zhong, S. L.; Zhang, D. L.; Bi, K.; Zhang, Y. X.; Zhao, Y.; Dang, Z. M. Flexible and Stretchable Capacitive Sensors with Different Microstructures. *Adv. Mater.* **2021**, *33*, No. 2008267.

(5) Li, H.; Gao, G.; Xu, Z.; Tang, D.; Chen, T. Recent Progress in Bionic Skin Based on Conductive Polymer Gels. *Macromol. Rapid Commun.* **2021**, *42*, No. e2100480.

(6) Li, H.; Liang, Y.; Gao, G.; Wei, S.; Jian, Y.; Le, X.; Lu, W.; Liu, Q.; Zhang, J.; Chen, T. Asymmetric Bilayer Cnts-Elastomer/Hydrogel Composite as Soft Actuators with Sensing Performance. *Chem. Eng. J.* **2021**, *415*, No. 128988.

(7) Wang, S.; Gao, Y.; Wei, A.; Xiao, P.; Liang, Y.; Lu, W.; Chen, C.; Zhang, C.; Yang, G.; Yao, H.; Chen, T. Asymmetric Elastoplasticity of Stacked Graphene Assembly Actualizes Programmable Untethered Soft Robotics. *Nat. Commun.* **2020**, *11*, No. 4359.

(8) Zhuo, S.; Zhao, Z.; Xie, Z.; Hao, Y.; Xu, Y.; Zhao, T.; Li, H.; Knubben, E. M.; Wen, L.; Jiang, L.; Liu, M. Complex Multiphase Organohydrogels with Programmable Mechanics toward Adaptive Soft-Matter Machines. *Sci. Adv.* **2020**, *6*, No. eaax1464.

(9) Jones, T. J.; Jambon-Puillet, E.; Marthelot, J.; Brun, P. T. Bubble Casting Soft Robotics. *Nature* **2021**, *599*, 229−233.

(10) Lee, W.-K.; Preston, D. J.; Nemitz, M. P.; Nagarkar, A.; MacKeith, A. K.; Gorissen, B.; Vasios, N.; Sanchez, V.; Bertoldi, K.; Mahadevan, L.; Whitesides, G. M. A Buckling-Sheet Ring Oscillator for Electronics-Free, Multimodal Locomotion. *Sci. Rob.* **2022**, *7*, No. eabg5812.

(11) De Pascali, C.; Naselli, G. A.; Palagi, S.; Scharff, R. B. N.; Mazzolai, B. 3D-Printed Biomimetic Artificial Muscles using Soft Actuators that Contract and Elongate. *Sci. Robot.* **2022**, *7*, No. eabn4155.

(12) Qiao, C.; Liu, L.; Pasini, D. Bi-Shell Valve for Fast Actuation of Soft Pneumatic Actuators via Shell Snapping Interaction. *Adv. Sci.* **2021**, *8*, No. e2100445.

(13) Li, S.; Zhang, R.; Zhang, G.; Shuai, L.; Chang, W.; Hu, X.; Zou, M.; Zhou, X.; An, B.; Qian, D.; Liu, Z. Microfluidic Manipulation by Spiral Hollow-Fibre Actuators. *Nat. Commun.* **2022**, *13*, No. 1331.

(14) Eger, C. J.; Horstmann, M.; Poppinga, S.; Sachse, R.; Thierer, R.; Nestle, N.; Bruchmann, B.; Speck, T.; Bischoff, M.; Ruhe, J. The Structural and Mechanical Basis for Passive-Hydraulic Pine Cone Actuation. *Adv. Sci.* **2022**, *9*, No. e2200458.

(15) Chun, S.; Kim, J.-S.; Yoo, Y.; Choi, Y.; Jung, S. J.; Jang, D.; Lee, G.; Song, K.-I.; Nam, K. S.; Youn, I.; Son, D.; Pang, C.; Jeong, Y.; Jung, H.; Kim, Y.-J.; Choi, B.-D.; Kim, J.; Kim, S.-P.; Park, W.; Park, S. An Artificial Neural Tactile Sensing System. *Nat. Electron.* **2021**, *4*, 429−438.

(16) Dicker, M. P. M.; Baker, A. B.; Iredale, R. J.; Naficy, S.; Bond, I. P.; Faul, C. F. J.; Rossiter, J. M.; Spinks, G. M.; Weaver, P. M. Light-Triggered Soft Artificial Muscles: Molecular-Level Amplification of Actuation Control Signals. *Sci. Rep.* **2017**, *7*, No. 9197.

(17) Blanpain, C.; Fuchs, E. Plasticity of Epithelial Stem Cells in Tissue Regeneration. *Science* **2014**, *344*, No. 1242281.

(18) Pittenger, M. F.; Mackay, A. M.; Beck, S. C.; Jaiswal, R. K.; Douglas, R.; Mosca, J. D.; Moorman, M. A.; Simonetti, D. W.; Craig, S.; Marshak, D. R. Multilineage Potential of Adult Human Mesenchymal Stem Cells. *Science* **1999**, *284*, 143−147.

(19) Yuk, H.; Lu, B.; Zhao, X. Hydrogel Bioelectronics. *Chem. Soc. Rev.* **2019**, *48*, 1642−1667.

(20) Liu, X.; Liu, J.; Lin, S.; Zhao, X. Hydrogel Machines. *Mater. Today* **2020**, *36*, 102−124.

(21) Keplinger, C.; Sun, J.-Y.; Foo, C. C.; Rothemund, P.; Whitesides, G. M.; Suo, Z. Stretchable, Transparent, Ionic Conductors. *Science* **2013**, *341*, 984−987.

(22) Madden, J. D. Mobile Robots: Motor Challenges and Materials Solutions. *Science* **2007**, *318*, 1094−1097.

(23) Rogers, J. A. A Clear Advance in Soft Actuators. *Science* **2013**, *341*, 968−969.

(24) Lee, J.; Tan, M. W. M.; Parida, K.; Thangavel, G.; Park, S. A.; Park, T.; Lee, P. S. Water-Processable, Stretchable, Self-Healable,

Thermally Stable, and Transparent Ionic Conductors for Actuators and Sensors. *Adv. Mater.* **2020**, *32*, No. e1906679.

(25) Rosset, S.; Shea, H. R. Flexible and stretchable electrodes for dielectric elastomer actuators. *Appl. Phys. A* **2013**, *110*, 281−307.

(26) Sarwar, M. S.; Dobashi, Y.; Preston, C.; Wyss, J. K. M.; Mirabbasi, S.; W, M. J. D. Bend, Stretch, and Touch: Locating a Finger on an Actively Deformed Transparent Sensor Array. *Sci. Adv.* **2017**, *3*, No. e1602200.

(27) Lee, H.; Um, D. S.; Lee, Y.; Lim, S.; Kim, H. J.; Ko, H. Octopus-Inspired Smart Adhesive Pads for Transfer Printing of Semiconducting Nanomembranes. *Adv. Mater.* **2016**, *28*, 7457−7465.

(28) Kranjec, J.; Beguš, S.; Geršak, G.; Drnovšek, J. Non-Contact Heart Rate and Heart Rate Variability Measurements: A review. *Biomed. Signal Process. Control* **2014**, *13*, 102−112.

(29) Walker, G. A Review of Technologies for Sensing Contact Location on the Surface of A Display. *J. Soc. Inf. Disp.* **2012**, *20*, 413−440.

(30) Yang, B.; Yu, C.; Dong, Y. Capacitively Coupled Electrocardiogram Measuring System and Noise Reduction by Singular Spectrum Analysis. *IEEE Sens. J.* **2016**, *16*, 3802−3810.